

Article

Modeling the Slump-Type Landslide Tsunamis Part I: Developing a Three-Dimensional Bingham-Type Landslide Model

Tso-Ren Wu ^{1,*}, Thi-Hong-Nhi Vuong ¹, Chun-Wei Lin ¹, Chun-Yu Wang ² and Chia-Ren Chu ²

¹ Graduate Institute of Hydrological and Oceanic Sciences, National Central University, Taoyuan 32001, Taiwan; hongnhi1017@g.ncu.edu.tw (T.-H.-N.V.); starynight2006@g.ncu.edu.tw (C.-W.L.)

² Department of Civil Engineering, National Central University, Taoyuan 32001, Taiwan; cywang@ncu.edu.tw (C.-Y.W.); crchu@ncu.edu.tw (C.-R.C.)

* Correspondence: tsoren@ncu.edu.tw; Tel.: +886-03-422-7151-65685

Received: 17 August 2020; Accepted: 11 September 2020; Published: 17 September 2020



Featured Application: This paper aims to develop a landslide model to simulate slump-type landslide tsunamis. The modified Bi-viscous model can be used to simulate the landslide movements in both the in-land area and ocean area. The model is able to describe the developments of the landslide as well as the slip surface. In addition, the model can be applied to hazard assessments.

Abstract: This paper incorporates Bingham and bi-viscosity rheology models with the Navier–Stokes solver to simulate the dynamics and kinematics processes of slumps for tsunami generation. The rheology models are integrated into a computational fluid dynamics code, Splash3D, to solve the incompressible Navier–Stokes equations with volume of fluid surface tracking algorithm. The change between un-yield and yield phases of the slide material is controlled by the yield stress and yield strain rate in Bingham and bi-viscosity models, respectively. The integrated model is carefully validated by the theoretical results and laboratory data with good agreements. This validated model is then used to simulate the benchmark problem of the failure of the gypsum tailings dam in East Texas in 1966. The accuracy of predicted flood distances simulated by both models is about 73% of the observation data. To improve the prediction, a fixed large viscosity is introduced to describe the un-yield behavior of tailings material. The yield strain rate is obtained by comparing the simulated inundation boundary to the field data. This modified bi-viscosity model improves not only the accuracy of the spreading distance to about 97% but also the accuracy of the spreading width. The un-yield region in the modified bi-viscosity model is sturdier than that described in the Bingham model. However, once the tailing material yields, the material returns to the Bingham property. This model can be used to simulate landslide tsunamis.

Keywords: landslide tsunamis; slumps tsunami; bingham rheology model; bi-viscosity model; VOF; slip surface; tailings dam; mudslide; Navier–Stokes; LES

1. Introduction

Tsunamis are potentially deadly and destructive sea waves. Most of the tsunamis are formed as a result of submarine earthquakes and submarine landslides. These landslides, in turn, are often triggered by earthquakes or volcanic eruptions [1]. Over the past 20 years, catastrophic tsunamis in Papua New Guinea (1998), Indian Ocean (2004), Japan (2011), Palu Bay Indonesia (2018), and Anak Krakatau Indonesia (2018) have driven major advances in understanding of earthquakes and submarine landslides as tsunami sources [2]. In fact, submarine landslides have become suspects in the creation

of the “silent tsunami” triggered by distant earthquakes. As exemplified by the 2018 Anak Krakatau Tsunami event, the tsunamis were initiated away from the epicentral area of an associated earthquake, or were far larger than expected given the earthquake magnitude. The silent tsunamis arrived without precursory seismic warning. They were generated by a landslide caused by the Anak Krakatau volcanic eruption. A landslide-generated tsunami may occur independently or along with an earthquake-generated tsunami, which can complicate the warning process and increase the losses [3]. Although the landslide-generated waves characteristically have shorter periods than the observed tsunami waves, the combination of the waves is able to produce long waves comparable with those observed, due to the ringing effects of the trapped waves inside a bay or coastal area [4].

The landslide can be classified as block collapse (slides) and sediment or mud collapse (slumps). The difference between them is mainly in the rigidity of the sliding body. Slides are landslides with rigid sliding bodies, and slumps are landslides with deformable sliding bodies [5–7]. The special consideration regarding this particular condition is to model the slump kinematics, based on the forces acting on the slump and the rheology of the slump materials. This study aims to develop a slump-type landslide model for the future study on landslide-generated tsunamis. In order to reduce the complexity, this paper shall focus on the developing a model to describe the kinematics and dynamics of pure landslides. After the model validation and sensitivity analyses, this model can be used to study the tsunamis generated by slumps. In terms of the pure landslide simulations, the failure of the gypsum tailings dam in East Texas in 1966 (FGT66) is one of the famous benchmark problems. FGT66 features a field-scale with a clean and simple geometry. In this study, the benchmark problem, FGT66, will be studied thoroughly to develop a reliable landslide model.

Similar to the slump-type landslide tsunami, the tailings are considered a fine material by Jing [8], Zhang [9], and Qiao [10]. Numerically, the slumps and tailings fluid can be considered a viscoplastic material with the yield stress, which is one of the important parameters. Mudflow can be modeled by Bingham model [11–13], Herschel–Bulkley model [14,15], and the Coulomb-viscoplastic model [16] by incorporating them with the depth-integrated equations models. The viscosity in these models is discontinuous [17]. The analytical solution was first proposed by Jeyapalan [18]. The behavior of tailings was described by the Bingham model (BM) [18]. A one-dimensional profile and a freezing time were provided [18]. Liu [12] studied a spreading flow of high concentration mud on an inclined plane. An analytical solution to a thin sheet of Bingham fluid was derived and verified with experimental data [12]. Huang [15] studied the spreading of a two-dimensional, unsteady mudflow on a steep slope. The nonlinear rheological properties of the mud were described by the Herschel–Bulkley model [15]. In their paper [15], the von Karman integral method was used to derive the depth-averaged continuity and momentum equations. The influences of shear-thinning on the free-surface profiles and spreading characteristics of the mudflow were discussed [15]. Pastor [19] implemented the Bingham model into a depth-averaged numerical model to simulate the hyper-concentrated flows. The bottom friction was approximated by a third-order polynomial function to save computational time [19]. Chen [20] developed a two-dimensional two-layer model to simulate the confluence of clear water and mudflow. They used the Harten scheme [21] to solve the depth-averaged equations and the Strang splitting method [22] to manage the friction term. The model was certified by comparing the simulation results with the prediction of Pastor [19]. Recently, Pudasaini [16] proposed a first-ever multi-mechanical, multi-phase mass flow model that employed pressure- and rate-dependent Coulomb-viscoplastic rheology, very flexible for the application to the wide range of geophysical mass flow.

Given the above studies, theoretical models or two-dimensional depth-averaged numerical models can be used to simulate mudflows in simplified conditions [6,8,11,12,15,16]. The depth-integrated model is simplified from Navier–Stokes equations by ignoring the vertical acceleration [23]. The depth-integrated model is suitable to predict the flow without strong vertical acceleration or a sharp velocity shearing [24]. The vertical acceleration and velocity shearing are important in the case of a slope with rugged topography or mudslide overtopping a structure. Inside a complex 3D flow structure, the tailings material will transfer from an un-yield/plug zone to a yield/liquefied/sheared zone if the

shear stress is greater than the yield shear stress. Before the tailings reach this plug zone, the liquefied zone might dominate the entire flow field due to strong shear. Adopting a three-dimensional rheology model is an alternative to fully and globally describe the strongly converging and diverging flows [19,20]. For more detailed results, solving the three-dimensional Navier–Stokes equations is recommended [21,22]. The Navier–Stokes equation modes were utilized to study a mudflow in the 1990s. Many of these studies concentrated on solving 2D problems [7,16,25]. With the advance of computers in the early twentieth century, the 3D Navier–Stokes equations were able to study a mudflow by smoothed particle hydrodynamics (SPH) method [22,26], and projection method [20,23,24].

The rheological properties are crucial issues in a slump or a tailings flow simulations. The slump or tailings fluid is a non-Newtonian fluid in nature [27] with complex rheological properties. The travel distance and the spreading of a slump or a tailings flow are affected by the rheological equation [28]. As for the determination of the rheological parameters, Henriquez [27] determined the yield stress and viscosity of tailings flow by using rheometer and slump tests. The mixture of different materials leads to a complex, yet not well understood rheological behavior [29]. Field observations of mudflow behavior and rheology are challenging and still rare. Numerical modeling is chosen when an assessment of mudflow behavior is needed for planning, zoning, and hazard assessment [28,30–32]. Most models require direct calibration to capture site-specific behavior. However, reliable calibration data are scarce, and laboratory experiments are difficult to be upscaled to field situations [29].

This study is divided into two parts. The first part, the main body of this paper, is to build a slump-type landslide model. The slump material is simulated as a homogeneous non-Newtonian material, whose behavior is described by the Bingham model, conventional bi-viscosity model, and modified bi-viscosity model. The failure of the gypsum tailings dam in 1966 is used for the model validation, calibration, sensitivity analysis. The free surface of the slump is tracked by the volume of fluid (VOF) [33] method. In the second part provided in the other paper, tsunamis are generated by a slump on a slope. The slump is described by Bingham model. The accuracy of model is validated by the laboratory data of Assier Rzadkiewicz [34].

The landslide tsunami can be excited by slump-type landslide which involves complex interactions between slumps, water, and air. In order to understand the phenomena more clearly, this study discusses the slump-type landslide in Part I and the tsunamis induced by a slump-type landslide in Part II. In Part I, the rheology models are discussed in detail to deeply understand the characteristics of each rheology parameter to the slump movement and deformation. In Part II, the tsunamis affected by those parameters will be discussed.

The next section gives an overview of the modeling approach. Section 3 presents the model validation with analytical solutions as well as experimental data. The study of the failure of the gypsum tailings dam in East Texas in 1966 is given in Section 4. Section 5 describes a series of sensitivity analyses on the yield strain rate and the grid resolution. Conclusions are made in Section 6.

2. Rheological Model and Numerical Algorithm

For flow rheology, the Bingham model (BM) has been widely used to simulate mudflows [4,29,35], lava flows [36], landslides [37], and multi-phase mass flows [16].

The rheological properties of BM can be presented as [38,39]:

$$\mu(\dot{\gamma}) = \begin{cases} \mu_A = \infty \text{ and } \dot{\gamma} = 0, & \text{if } \tau < \tau_y \\ \mu_B + \frac{\tau_y}{\sqrt{\frac{1}{2}\dot{\gamma}_{ij}\dot{\gamma}_{ij}}} \text{ and } \dot{\gamma} > 0, & \text{if } \tau \geq \tau_y \end{cases} \quad (1)$$

where μ_A is the viscosity of the un-yield region, μ_B is the viscosity of the yield zone, τ_y is the yield stress, and $\dot{\gamma}_y$ is the yield strain rate, $\dot{\gamma}_{ij} = \frac{\partial u_i}{\partial x_j} + \frac{\partial u_j}{\partial x_i}$. The symbol $\dot{\gamma}$ is the second invariant of the $\dot{\gamma}_{ij}$, which is defined as $\dot{\gamma} = \sqrt{\frac{1}{2}\dot{\gamma}_{ij}\dot{\gamma}_{ij}}$.

Even with the simplicity of the BM, the stress is still indeterminate in the un-yield region, which means the exact shape and location of the yield surface(s) cannot be determined [40]. To remedy this drawback in the present work, the conventional bi-viscosity model (CBM) [41] was adopted. This idea allows a small deformation to occur in the un-yield region(s) by treating it as an extremely high viscosity fluid. In the yield region, the material is considered a Bingham fluid. This method makes it possible for the stress to be computable in the whole domain, including the un-yield region so that the location of the yield surface can be easily determined [40].

The rheological properties of CBM can be presented as [42,43]:

$$\mu(\dot{\gamma}) = \begin{cases} \mu_A = \frac{\tau_y}{\dot{\gamma}_y}, & \text{if } \dot{\gamma} < \dot{\gamma}_y \\ \mu_B + \frac{\tau_y}{\sqrt{\frac{1}{2}\dot{\gamma}_{ij}:\dot{\gamma}_{ij}}}, & \text{if } \dot{\gamma} \geq \dot{\gamma}_y \end{cases} \quad (2)$$

Mathematically speaking, when $\dot{\gamma}_y$ approach zero, the CBM approaches BM. If the chosen $\dot{\gamma}_y$ is sufficiently small, we can practically replace the un-yield region viscosity with a higher viscosity. This guarantees that a viscous solver can handle the determination of the shape and the location of the plug surface [40].

However, a mud material will become sturdy when experiencing compaction or tamping processes experiencing. To describe the sturdy behavior in the plug zone, a larger μ_A and a larger $\dot{\gamma}_y$ are required. The larger μ_A plays a role of keeping the rigid shape. The larger $\dot{\gamma}_y$ indicates that the material can sustain a large shear stress without deformation. To achieve that effect, the modified bi-viscosity model (MBM) is born and written as:

$$\mu(\dot{\gamma}) = \begin{cases} \mu_A > \frac{\tau_y}{\dot{\gamma}_y}, & \text{if } \dot{\gamma} < \dot{\gamma}_y \\ \mu_B + \frac{\tau_y}{\sqrt{\frac{1}{2}\dot{\gamma}_{ij}:\dot{\gamma}_{ij}}}, & \text{if } \dot{\gamma} \geq \dot{\gamma}_y \end{cases} \quad (3)$$

In this model, the yield stress τ_y and yield viscosity μ_B of the mud material are exponentially dependent on material concentration [44]. The detailed descriptions are added in Section 5.2. To present the un-yield behavior, μ_A is chosen to be infinite based on the suggestions of Assier Rzakiewicz [34], Taibi [45], and Yu [28]. In this paper, the infinite number of viscosity $\mu_A = 10^{10}$ Pa s is chosen by the sensitivity analysis. The values of yield strain rate $\dot{\gamma}_y$ are also discussed in Section 5.2. $\dot{\gamma}_y = 0.2 \text{ s}^{-1}$ is adopted by a sensitivity analysis to illustrate the deformation in MBM.

The viscoplastic models, BM, CBM, and MBM, were coupled with the Splash3D model. The Splash3D model was renovated from the open-source software, Truchas, which was originally developed by Los Alamos National Laboratory [46]. The original program can simulate the incompressible flows with multi-fluid interfaces. The code solves three-dimensional continuity and Navier–Stokes equations by adopting the projection method [36,37,47] and the finite volume discretization method [48]. The Splash3D model was enhanced with several hydrodynamic modules such as the large eddy simulation (LES) turbulence module [40,49], and the moving-solid module [50] to deal with breaking waves and wave–obstacle interaction problems. Readers are encouraged to read the reference Chu [50] for the detailed numerical algorithm. In this study, the Splash3D is developed with the rheological model to solve mudflow problems. The fundamental governing equations are continuity and momentum equations:

$$\frac{\partial \bar{u}_i}{\partial x_i} = 0 \quad (4)$$

$$\frac{\partial}{\partial t}(\rho \bar{u}_i) + \frac{\partial}{\partial x_j}(\rho \bar{u}_i \bar{u}_j) = -\frac{\partial \bar{P}}{\partial x_i} + \frac{\partial}{\partial x_j} \left[\mu_e \left(\frac{\partial \bar{u}_i}{\partial x_j} + \frac{\partial \bar{u}_j}{\partial x_i} \right) \right] + \rho g_i \quad (5)$$

where the subscripts $i, j = 1, 2, 3$ represent the x, y, z directions respectively; t is the time, u is the velocity; P is the pressure; the over-bar represents the spatially filtered value [51]; g is the gravitational acceleration; ρ is the density; and μ_e is the effective viscosity.

Under the influence of gravity, tailings flow out of the break at a high speed and might be in a turbulent state [52]. In this study, the large eddy simulation (LES) [53] is adopted to address the turbulence effect. The effective viscosity μ_e is defined as:

$$\mu_e = \mu(\dot{\gamma}) + \mu_t \tag{6}$$

where $\mu(\dot{\gamma})$ is the rheological viscosity of mud and μ_t is the viscosity of the sub-grid scale turbulence.

The Smagorinsky model [53] relates the residual stress to the rate of filtered strain. Based on the dimensional analysis, the subgrid-scale eddy viscosity is modeled as:

$$\mu_t = \rho l_s^2 \bar{S} = \rho (C_s \Delta)^2 \bar{S} \tag{7}$$

where l_s is the Smagorinsky length scale, which is a product of the Smagorinsky coefficient C_s and the filter width Δ ; \bar{S} is the characteristic filtered rate of strain:

$$\bar{S} = \sqrt{\frac{1}{2} \dot{\gamma}_{ij} \dot{\gamma}_{ij}} \tag{8}$$

In general, C_s varies from 0.1 to 0.2 in different flows. The present simulations use a value of 0.15. Δ is the filter width. Infinite volume discretization Δ is the grid size:

$$\Delta = (\Delta x_1 \times \Delta x_2 \times \Delta x_3)^{1/3} \tag{9}$$

where $\Delta x_1, \Delta x_2, \Delta x_3$ are the three components of the grid lengths.

In the present model, the tailings fluid is treated as a single homogeneous mud material. The tailings fluid and air are assumed to be two incompressible and non-immiscible fluids. The free-surface between the tailings fluid and air is tracked by the volume of fluid (VOF) method [54]. The volume fraction, f_m , is used to describe the fraction of the m th material in each cell. The volume fraction f_m varies in $[0,1]$ and should sum to unity everywhere. $f_m = 1$ if the cell is fully occupied by the m th material; $0 < f_m < 1$ if the cell contains the interfaces of the m th material; $f_m = 0$ if the cell contains no m th material. The VOF equation is given by Equation (10):

$$\frac{\partial(f_m)}{\partial t} + \nabla \cdot (u_i f_m) = 0 \tag{10}$$

In this study, the interfaces between different materials are solved by the VOF method. Because the fundamental assumption of the VOF method is that each fluid is immiscible, there is no difference in terms of the VOF equations between subaerial or submerged slumps. For both the subaerial and submerged (underwater) slumps, the VOF method is briefly described here [50,55,56].

Two stability conditions of dt need to be satisfied while solving Navier–Stokes equations:

$$dt_c < C_r \frac{dl}{Max(|\mathbf{u}|)} \tag{11}$$

$$dt_\mu < V_\mu \frac{(dl)^2}{Max(\mu_{eff})} \tag{12}$$

where dt_c is the time step restricted by the advection term, C_r is Courant number, which is defined as $C_r = Max(|\mathbf{u}|)dt/dl$, dl is the measure of the cell size, dt_μ is the time step restricted by the diffusion term, V_μ is the viscous number, which is defined as $V_\mu = Max(\mu_{eff})dt/(dl)^2$.

When the viscosity is large in the un-yield zone [50,57,58], the time-step dt_μ is very small, which might lead to the numerical divergence or even a crash in the solution procedure [59]. However, this small time-step restriction can be relaxed by adopting the implicit scheme. The viscous implicitness θ is used to calculate the velocity \mathbf{u} at the time level n , and $\mathbf{u}^\theta = (1 - \theta)\mathbf{u}^n + \theta\mathbf{u}^{n+1}$. In this study, θ is given as unity, which implies a fully implicit treatment, and dt_μ is no longer restricted by Equation (12).

The algorithm of Splash3D solves equations of conservation of mass and momentum for any number of immiscible, incompressible fluids, and tracks the interfaces between them. Except for adding a water body to the computational domain in Part II to simulate slump-type landslide tsunamis, no additional numerical adjustment is required from Part I to Part II. Therefore, the findings in Part I can be applied to the underwater modeling in Part II. To simplify the complexity from the slump, water, and air, the slump-type landslide in the dry-land area, FGT66, is adopted in Part I for a better understanding of the model characteristics. The same numerical model will be applied to study the FGT66 in Part I and slump-type landslide tsunamis in Part II.

To summarize the numerical method, this paper adopts Splash3D model to solve the conservation and Navier–Stokes equations for any number of immiscible, incompressible fluids. The LES turbulence model with Smagorinsky closure is used to add the effect from turbulence flow field. The VOF method is adopted to track the interfaces between each fluid including slumps. The new contributions from this study in terms of the numerical modeling are incorporating the BM, CBM, and MBM into the Splash3D model with the implicit scheme to solve the slump material with a large viscosity number.

3. Validation

Two cases of mudflows are simulated for the model validation. The results are compared with both analytical solutions and laboratory experiment data.

3.1. Bingham Fluid Driven by Pressure Gradients

Byron–Bird [49] derived analytical solutions for the Bingham flow in a channel, driven by a pressure gradient $P_0 - P_L$. The channel was depicted as the length L and the width $2B$. The no-slip boundary condition was applied to the surfaces of the channel (Figure 1).

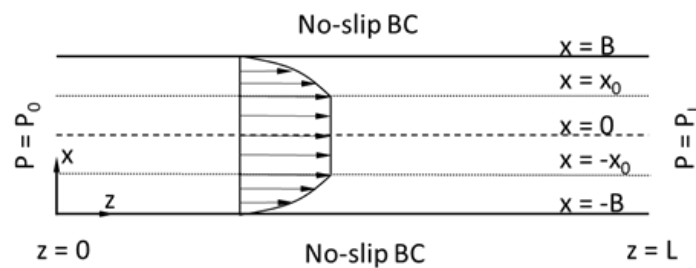


Figure 1. Flow in a channel driven by the pressure gradient, showing the plug region $-x_0 \leq x \leq x_0$ and the liquefied region $x_0 < x \leq B$ and $-B \leq x < -x_0$, based on Byron-Bird [49].

The yield surface is located at $x = x_0$ where $x_0 = \frac{\tau_0 L}{P_0 - P_L}$. The velocities in the plug region $v_z^>$, and in the liquefied region $v_z^<$ are:

$$v_z^> = \frac{(P_0 - P_L)B^2}{2\mu_B L} \left[1 - \left(\frac{x_0}{B} \right)^2 \right] - \frac{\tau_0 B}{\mu_B} \left[1 - \frac{x_0}{B} \right] \quad (-x_0 \leq x \leq x_0) \tag{13}$$

$$v_z^< = \frac{(P_0 - P_L)B^2}{2\mu_B L} \left[1 - \left(\frac{x}{B} \right)^2 \right] - \frac{\tau_0 B}{\mu_B} \left[1 - \frac{x}{B} \right] \quad (x_0 < x \leq B \text{ and } -B \leq x < -x_0) \tag{14}$$

if $\tau_0 = 0.0$, $x_0 = 0.0$, and the material is a Newtonian fluid.

Four cases were proposed to validate the models with Equations (13) and (14). They are one Newtonian case and three Bingham cases with different parameters such as channel length L , channel

width $2B$, one end's pressure P_0 , Bingham viscosity μ_B , and yield stress τ_0 . Figure 2 shows good agreements between the theoretical and numerical results of the all runs. One of the important features of a Bingham fluid is the plug zone (Figure 2b–d), which cannot be seen in the Newtonian fluid (Figure 2a). Note that the velocity of a Bingham fluid is constant in the plug region. In this region, the rate of change of velocity (strain rate) is equal to zero. In the liquefied region, the strain rate is greater than zero and the stress–strain relation of the fluid is dependent on the plastic viscosity μ_B . These figures demonstrate that the present numerical model can accurately describe the rheological behavior of Bingham fluids.

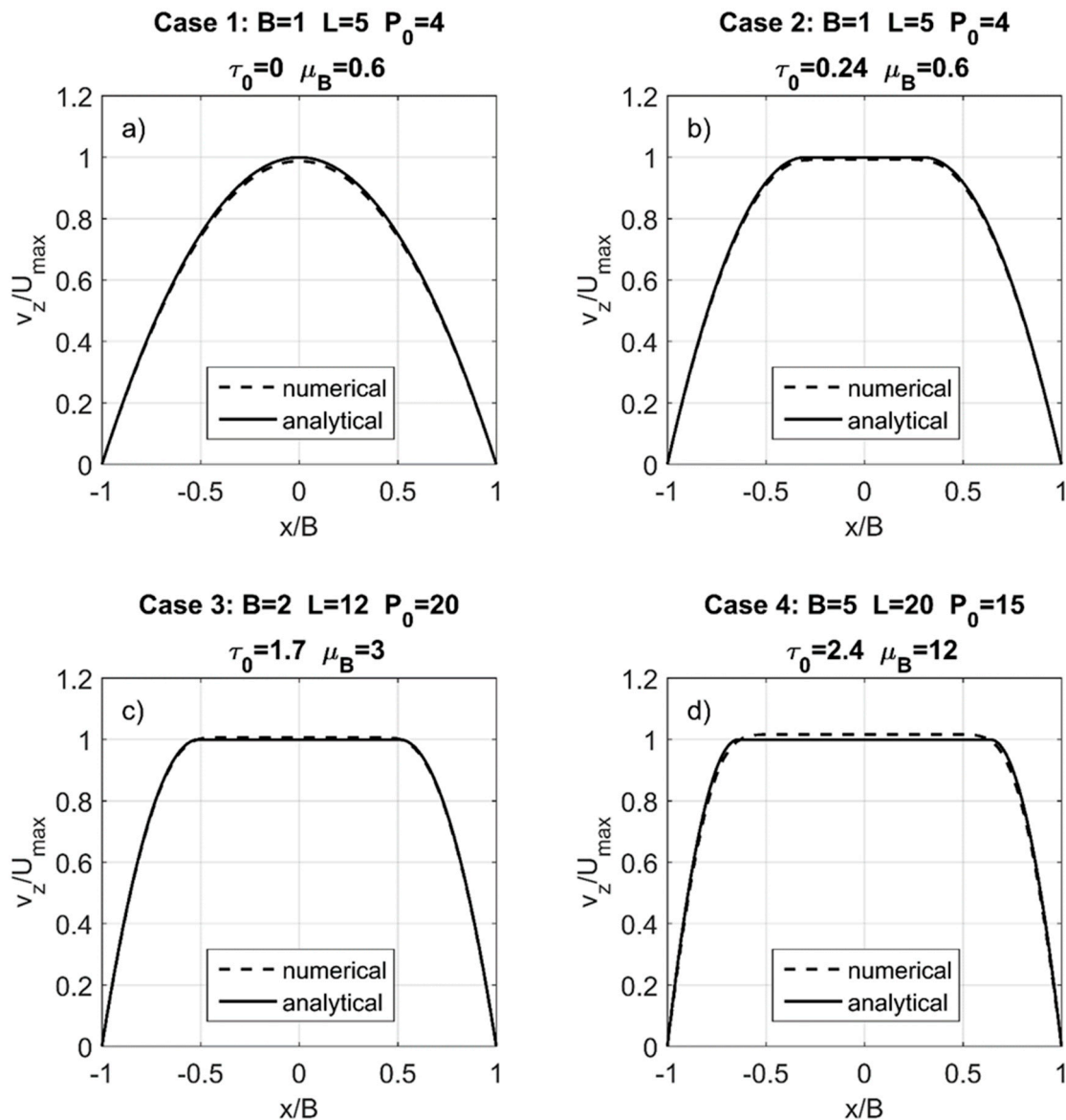


Figure 2. Validation of velocity profiles in a channel. (a) Newtonian fluid; (b–d) Bingham fluids with different parameters. The dashed lines are the numerical results. The solid lines are the analytical solution from Byron-Bird [49].

3.2. Spreading of Bingham Fluid on an Inclined Plane

The validation of the spreading of Bingham fluid on an inclined plane is set up based on the experiment of Liu [12]. Kaolinite was mixed with tap water to represent the mud. The mud was put in a reservoir. When the adjustable gate was opened, the mud flowed down onto an inclined dry bed

with the inclined angle $\theta = 0.9^\circ$. In this validation case, the openness of the gate was $H = 0.0051$ m. The fluid density $\rho = 1106 \text{ kg m}^{-3}$, the yield stress, $\tau_y = 0.875 \text{ Pa}$, the viscosity of the plug zone, $\mu_A = 10^{10} \text{ Pa s}$, the viscosity of liquefied zone, $\mu_B = 0.034 \text{ Pa s}$. A two-dimensional numerical domain was set up as $3.5 \times 0.2 \text{ m}$ (Figure 3) and was discretized into a regular mesh with grid size $dx = 2.3$, $dz = 2.0 \text{ mm}$. Figure 4a shows the spreading of mud on an inclined plane versus time. Figure 4b shows that the numerical result of Bingham model matches well with the theoretical solution as well as the experimental data from Liu [12]. The mudflow develops into a self-similar front when time $t > 8.0$ s. Because of the yield stress, the free surface needs not to be horizontal when the mud fluid is in static equilibrium, nor parallel to the plane bed when it reaches a steady-state. The mud front, like a steady gravity current, eventually advances at a constant speed with the same profile when there is a steady upstream discharge of mud [12]. The numerical results present a similar pattern of analytical solutions to that in Liu [12].

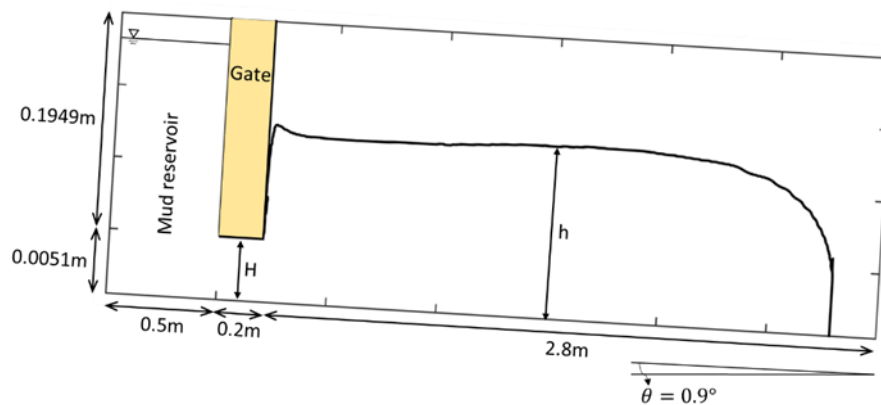


Figure 3. Numerical setup of Bingham flow on an inclined plane based on the experiment of Liu [12].

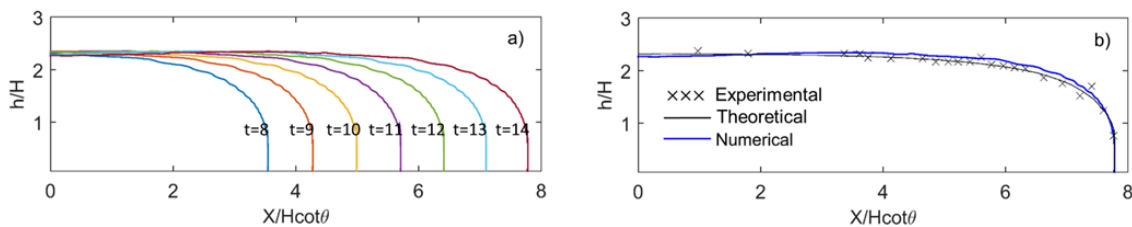


Figure 4. The free-surface profiles of Bingham flow on an inclined plane. (a) Snapshots (unit: s); (b) validation at $t = 14$ s. The experimental data and theoretical results are obtained from Liu [12]. The numerical results are simulated by the Bingham model.

4. Case Study—The Failure of the Gypsum Tailings Dam in East Texas in 1966 (FGT66)

4.1. Numerical Setup

The present numerical model was applied to simulating the failure of the gypsum tailings dam in East Texas in 1966 (FGT66). The reservoir was a rectangular shape and reached a height of 11 m when the failure took place. The slide was triggered by seepage at the toe of the embankment. An estimated 80,000–130,000 m^3 of gypsum was released in this flow failure. The released material traveled about 300 m before it came to a stoppage, with an average velocity of 2.5–5.0 m/s [60]. In this paper, the numerical setup was composed based on the geometry reported by Jeyapalan [60], shown in Figure 5. The size of the tailings reservoir was $280 \times 110 \times 11 \text{ m}$, and the breach was 120 m long. The center cross-section of the breach was located at $y = 220 \text{ m}$. The computational domain (510 in length, 400 in width, and 12 m in height) was discretized into a uniform mesh with a grid size $dx = 2.0$, $dy = 2.0$, $dz = 1.0 \text{ m}$. The number of the grid was 612,000. The bottom boundary (at $z = 0 \text{ m}$) was a no-slip boundary condition. The downstream ($x = 400 \text{ m}$) and lateral boundaries ($y = 0$ and $y = 400 \text{ m}$)

were free-slip walls. The downstream and lateral boundaries would not affect the simulation results because the domain was set to be much larger than the predicted tailing pattern. The gypsum tailings material was expected as a Bingham material. Based on the parameters reported by Jeyapalan [60], Pastor [61], and Chen [20], the yield stress of the tailings was $\tau_y = 10^3$ Pa, the viscosity of the liquefied zone was $\mu_B = 50$ Pa s, and the density was $\rho = 1400$ kg m⁻³. The viscosity of the plug zone was suggested to be infinite (e.g., $\mu_A = 10^{10}$ Pa s) by Assier Rzadkiewicz [34], Taibi [45], and Yu [28].

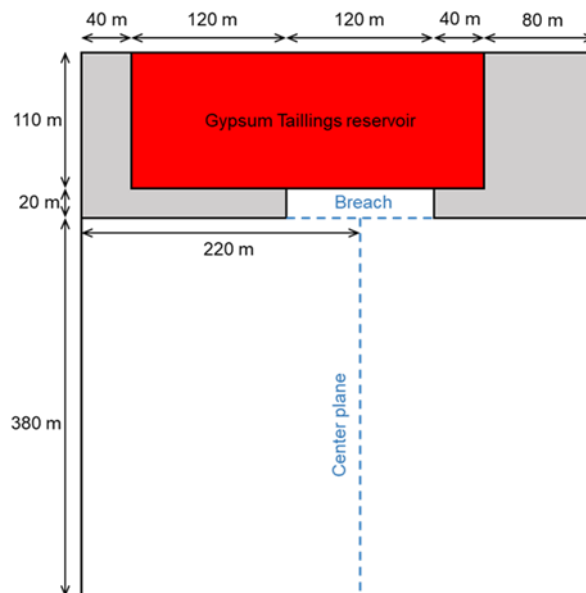


Figure 5. Numerical setup of the failure of the gypsum tailings dam in East Texas in 1966 (FTG66) based on the geometry reported in Jeyapalan [60].

4.2. The Results from Three Different Rheological Models

In this study, three different rheological models, Bingham Model (BM), Conventional Bi-viscosity Model (CBM), and Modified Bi-viscosity model (MBM) are employed to simulate the FTG66, as shown in Figures 6 and 7a. In the result from BM (Figure 6a), the mud thickness reduces gradually from the breach to the downstream toe. A sliding mud body is thicker in the breach center area. BM can simulate the stoppage of the material at about $t = 90$ s. The second result is obtained from CBM. The result in Figure 6b,c is produced by CBM with $\dot{\gamma}_y = 1 \times 10^{-4}$ s⁻¹ and $\dot{\gamma}_y = 2 \times 10^{-1}$ s⁻¹, respectively. In the CBM results, a high viscosity number is used to represent the un-yield phase, and a low viscosity number is used to represent the yield phase. The tailings shapes are similar between results of $\dot{\gamma}_y = 1 \times 10^{-4}$ s⁻¹ (Figure 6b) and $\dot{\gamma}_y = 2 \times 10^{-1}$ s⁻¹ (Figure 6c). They are also similar to those in the BM result (Figure 6a). However, the mud profiles at the center streamline are slightly different. The 'ridge' in the center of the breach (Figure 6b) is replaced by a relatively smooth hump (Figure 6c). In Figure 6, the results from CBM were nearly identical to those from BM. The flood distances predicted by BM and CBM were about 220 m. Compared to the field observation [60], the error of the predicted flood distance was about 27%. The field photo (Figure 7b) shows that the flood boundary was longer and narrower than the simulated results from BM and CBM. This might result from the sturdy behavior in the un-yield region. This sturdy behavior can be reached by increasing the un-yield viscosity μ_A and yield strain $\dot{\gamma}_y$. In this study, the un-yield viscosity $\mu_A = 10^{10}$ Pa s was chosen by the suggestion of Assier Rzadkiewicz [34], Taibi [34], and Yu [28]. The yield strain rate was chosen to be $\dot{\gamma}_y = 2 \times 10^{-1}$ s⁻¹ by matching the flood distance. Figure 7a shows the simulation of the deposited tailings from MBM. The flood distance at the freezing time $t = 110$ s was 310 m, which was 97% accurate to the filed data [60]. The result from MBM also showed a longer and narrower shape. However, it shall be noted that the white line segments in the aerial photo (Figure 7b) were not the elevation contour lines. The white line segments represent

the horizontal displacement of the gypsum tailings. They also indicate that the velocities along the central streamline were faster than those in the other regions. An indirect validation can be seen in the free-surface velocity profile, shown in Figure 9 at $t = 30$ s. However, the free-surface velocity will gradually reduce to zero as the freezing time is approaching.

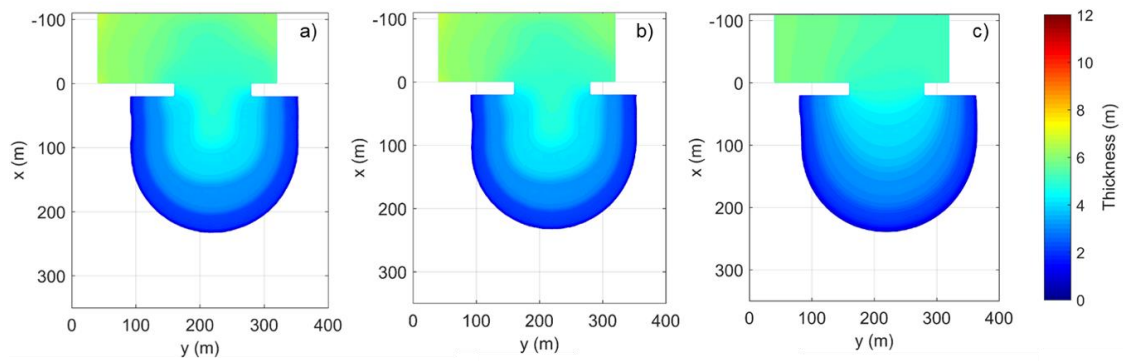


Figure 6. The free-surface profiles of tailings (a) by Bingham model (BM) with $\dot{\gamma}_y = 0.0 \text{ s}^{-1}$, (b) by conventional bi-viscosity model (CBM) with $\dot{\gamma}_y = 1 \times 10^{-4} \text{ s}^{-1}$, (c) by conventional bi-viscosity model (CBM) with $\dot{\gamma}_y = 2 \times 10^{-1} \text{ s}^{-1}$.

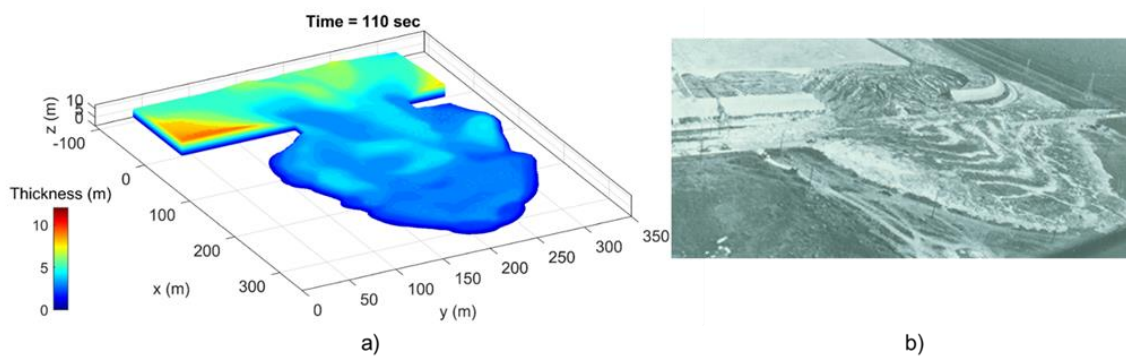


Figure 7. The free-surface profile of tailings. (a) The simulated modified bi-viscous model (MBM) at the stoppage $t = 110$ s; (b) the aerial photo of the FGT66 [60].

Figures 8 and 9 show the time evolution of the free-surface velocity of the mudflows from $t = 0 \sim 110$ s by using BM and MBM, respectively. The velocity at the early stage (about $t = 0 \sim 10$ s) of BM was higher than that of MBM. However, the simulated mudflow in BM stopped earlier (around 70–90 s). The surface velocity gradually approached zero from $t = 70$ s, and the flow came to a full stop at $t = 90$ s. The gypsum tailings distance was around 220 m, and the mean velocity was around $2.4 \sim 3.1 \text{ m s}^{-1}$ as shown in Figure 8. On the other hand, the flood distance from MBM was 310 m which was much closer to the field observation of 300 m [60]. The larger un-yield viscosity and yield strain rate limited the flood velocity at the early stage of the event (Figure 9). The mud started to liquefy and collapse in a small region near the breach in the first 10 s. The spreading shape of the tailings was symmetric along the centerline of the breach during $t = 0 \sim 20$ s. Because the supply of the tailings from the impoundment was asymmetric, the spreading shape gradually became asymmetric when $t > 20$ s. The maximum velocity of the released tailings occurred at $t = 30$ s. Then, the flow velocity gradually decreased. After $t = 90$ s, the tailings slowed down and stopped moving at $t = 110$ s. The mean velocity of the tailings flow was estimated at around $2.8 \sim 3.4 \text{ m s}^{-1}$.

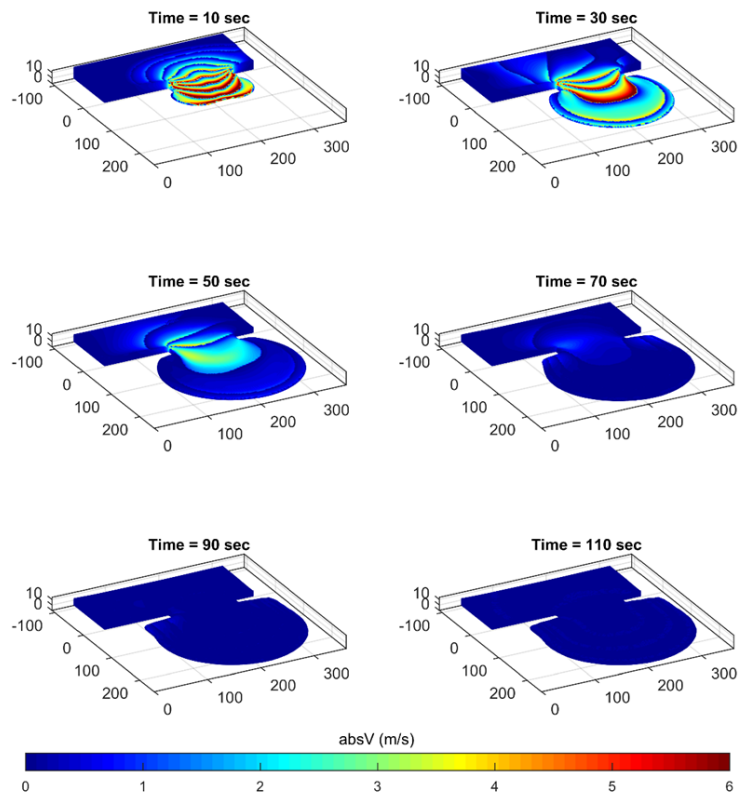


Figure 8. Snapshots of free-surface velocity profiles simulated by BM.

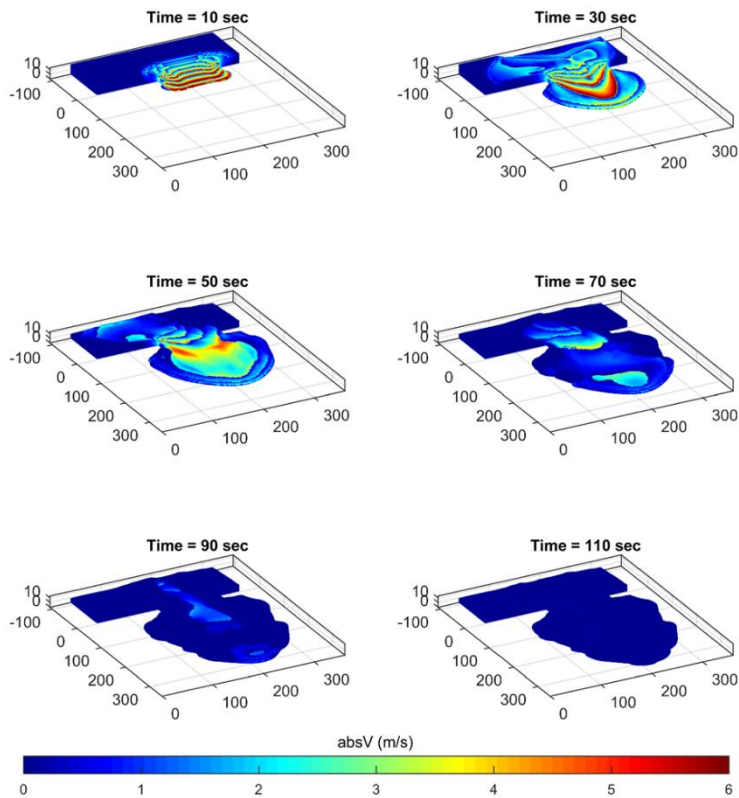


Figure 9. Snapshots of free-surface velocity profiles simulated by MBM.

The observation and simulation results of inundation distance, freezing time, and mean velocity provided in this study, as well as some historical studies, are listed in Table 1 for comparisons. The simulation results of the MBM were not only accurate in the freezing time and the mean velocity, but also in the inundation distance.

Table 1. The summary key values in the case of FGT66.

	Inundation Distance (m)	Freezing Time (s)	Mean Velocity (m s ⁻¹)
Observed values [60]	300	60~120	2.5~5.0
Theoretical results from charts [60]	550	132	4.2
Jeyapalan [60]	670	116	6.0
Pastor [19]	330	120	2.75
Chen [20]	360	120	3.0
Bingham model (Figure 8)	220	70~90	2.4~3.1
Modified bi-viscosity model (Figure 9)	310	90~110	2.8~3.4

Figure 10 shows the strain rate and the un-yield/yield zones of MBM results in the center cross-section of the breach ($y = 220$ m). The vertical axis was ten times exaggerated. The yield strain rate $\dot{\gamma}_y = 0.2 \text{ s}^{-1}$ was chosen to identify the interface between the un-yield/yield zones. The liquefied zone was located at the breach's front when $t = 10$ s, due to the large strain rate caused by gravitational force. The liquefied zone gradually shifted to the ground region after $t = 10$ s, resulting from the large shear stress that occurs near the bottom. However, the neighboring areas remained un-yield. The interface between the un-yield and yield zone was presented during the period of 10–40 s. It was caused by the viscosity's discontinuity of un-yield and yield zones. At $t = 90$ –110 s, the liquefied zone shrank gradually and disappeared at $t = 110$ s, due to the zero velocity in the entire flow field. This zero-velocity phenomenon was very close to the real landslide situation in which the velocity ceases to zero eventually.

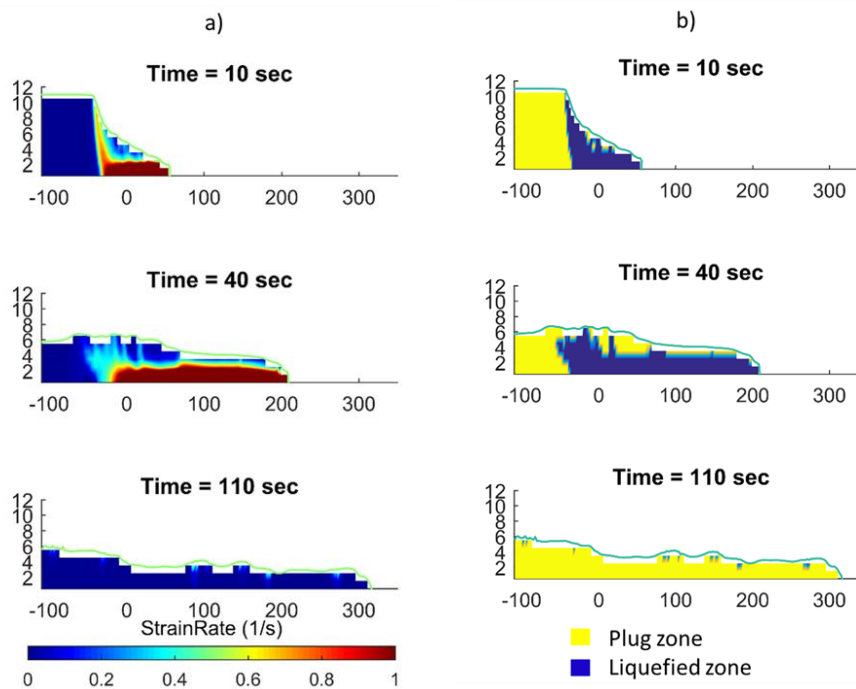


Figure 10. Snapshots on the centerline cross-section of the breach ($y = 220$ m) predicted by MBM. (a) The profiles of strain rate. The color bar is set from 0.0 to 1.0 s⁻¹ to emphasize the interface between the plug zone and liquefied zone at $\dot{\gamma}_y = 0.2 \text{ s}^{-1}$. (b) The discontinuity of the plug zone and liquefied zone.

4.3. Difference between the BM and MBM

Figure 11 shows the velocity magnitude profiles obtained from BM and MBM in the centerline cross-section ($y = 220$ m). In the BM results, the tailings moved faster than that in MBM. The maximum velocity of the tailings' front at $t = 10$ s was approximately $6.0\text{--}8.0$ m s^{-1} and decreased sharply during $t = 10\text{--}40$ s. It made the inundation distance (around 220 m) at $t = 110$ s shorter than that in MBM. In the MBM results, the maximum moving velocity was about $5.0\text{--}7.0$ m s^{-1} , which was slightly smaller than that in the results of BM. However, the MBM tailings flow took a longer time to reach the zero-velocity stage and the resulting inundation distance was longer than that in the BM results. The inundation distance (310 m) predicted by MBM was very close to the field observed (300 m). The yield strain rate played an important role in MBM. As long as the strain rate was smaller than the yield strain rate, a large viscosity was applied to slowing down the deformation. Due to the absence of measuring techniques, the yield strain rate in this study was obtained from the sensitivity analysis by taking the flood distance from the field observation as the criterion.

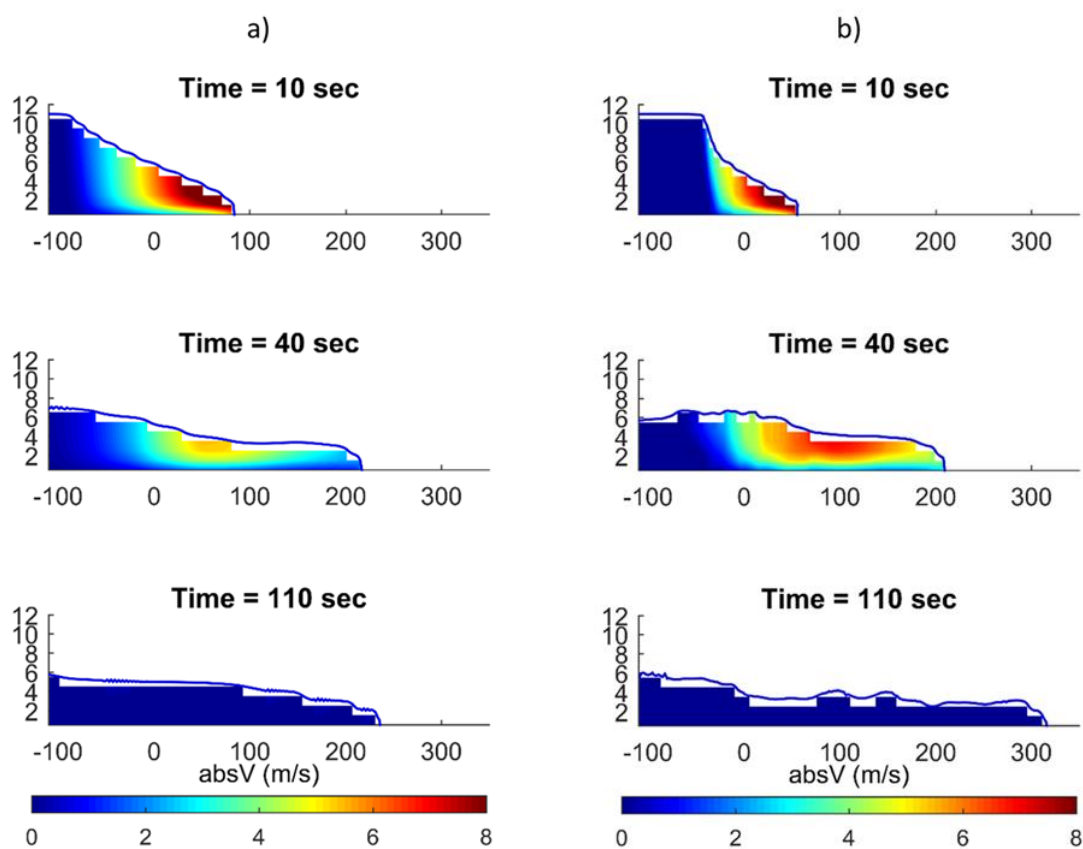


Figure 11. Snapshots of velocity magnitude on the centerline cross-section of the breach ($y = 220$ m) (a) Bingham model (BM); (b) modified bi-viscosity model (MBM).

Figure 12 illustrates the strain rate profile of the initiation process of the tailings flow. The strain rate profiles in BM results showed a smooth and continuous feature. A large amount of tailing material deformed and slid down (Figure 12a). On the other hand, in MBM results, the yield strain rate $\dot{\gamma}_y = 0.2$ s^{-1} was introduced as the indicator to identify the plug and sheared zone. Because the un-yield viscosity $\mu_A = 10^{10}$ Pa s was much greater than $\tau_y/\dot{\gamma}_y$, a discontinuous pattern of the strain rate could be observed in Figure 12b. The yield strain rate $\dot{\gamma}_y = 0.2$ s^{-1} kept the plug zone rigid. The initiation process of the mudslide in MBM results was different from that in BM results. A high strain rate appeared not only near the toe of the breach but also in the gate area, which caused the sliding process and formed a slip surface. The slip surface was the interface between the un-yield and

yield regions. In the bank of homogeneous mud, the slip surface of failure could be determined by the empirical method, which follows the arc of a circle that usually intersects the toe of the bank [52,53]. However, the slip surface was developed automatically by MBM. It is worth a more profound study in the future.

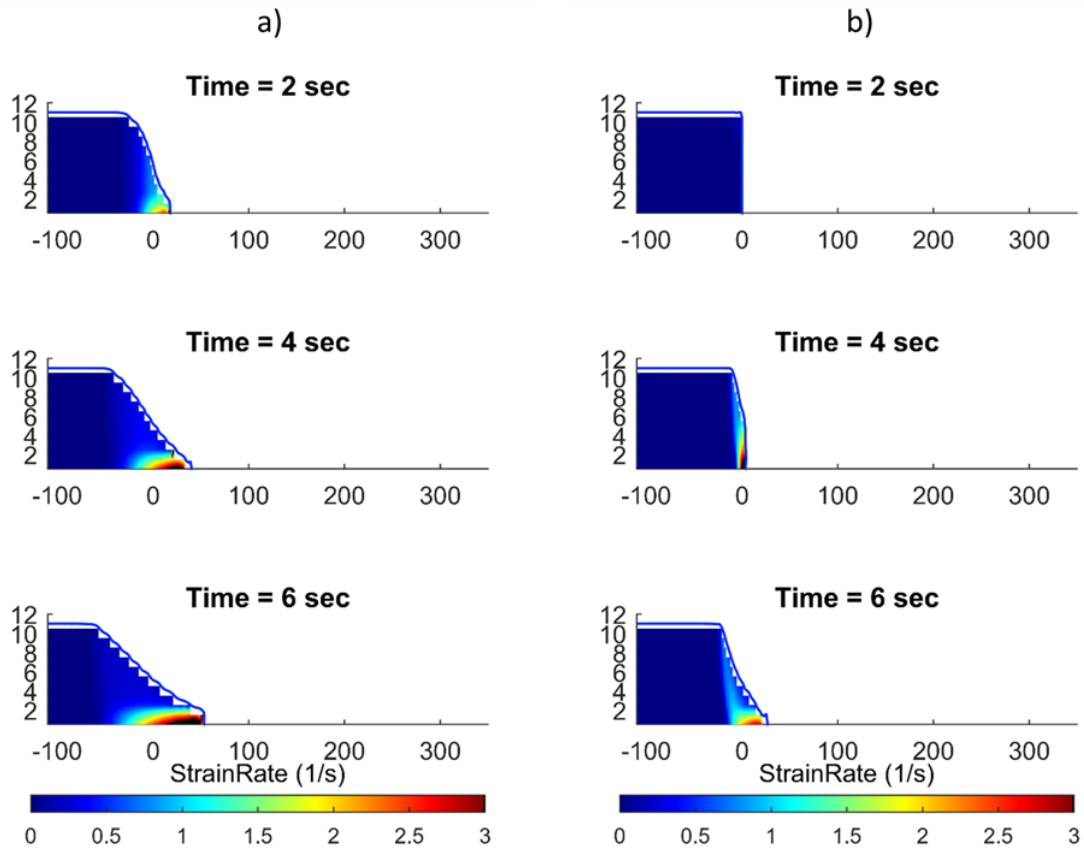


Figure 12. Snapshots of strain rate profile at the early stage on the centerline cross-section of the breach ($y = 220$ m). (a) Bingham model (BM); (b) modified bi-viscosity model (MBM).

Figure 13 shows the strain rate profiles of BM and MBM. The slip surface (Figure 13b) at $t = 10$ s and the interface between the plug/sheared zones (Figure 13b) at $t = 40$ s can be identified in the results of MBM. The slip surface was relatively sharp in the MBM results compared to the ones in MB (Figure 13a).

Because of adopting the larger un-yield viscosity μ_A , larger yield strain rate $\dot{\gamma}_y$, same yield stress τ_y , and same yield viscosity μ_B to simulate the FGT66, the un-yield zone of tailings in MBM was sturdier than that in the BM. However, once tailings yielded, the rheology returned to the conventional Bingham properties.

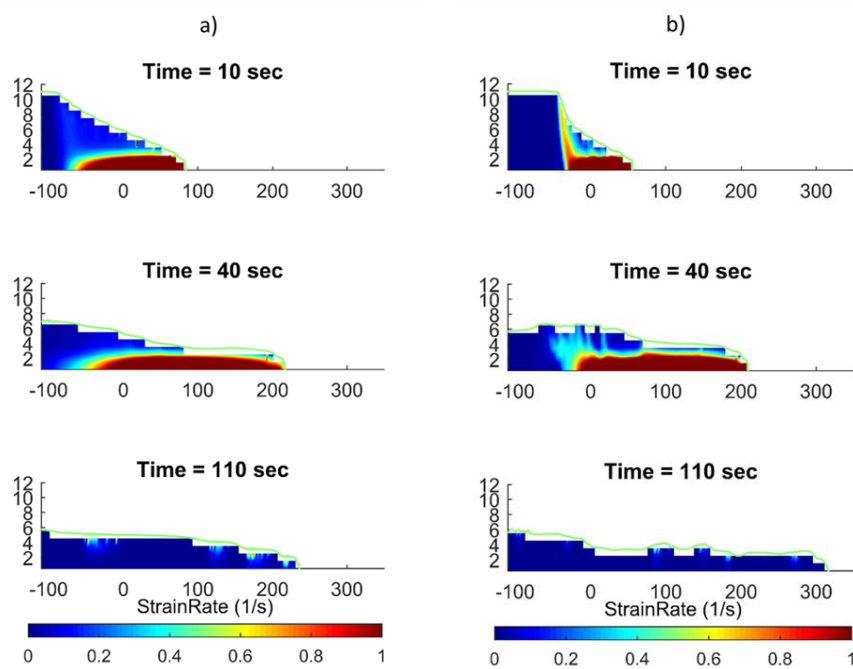


Figure 13. Snapshots of strain rate profile on the centerline cross-section of the breach ($y = 220$ m). (a) Bingham model (BM); (b) modified bi-viscosity model (MBM).

5. Discussion

5.1. The Role of the Grid Resolution

The grid resolution was a key factor in the strain rate calculation. To understand the sensitivity of the grid resolution of the flood distance, three cases of BM and nine cases of MBM were performed with the resolutions varying from dx : 1.8–2.2, dy : 1.8–2.2, and dz : 0.8–1.2 m. Figure 14 shows the deposited boundary of the tailings predicted by BM and MBM. The results show that BM was less sensitive to the resolution than MBM. The results from MBM show that the deposited boundary was more sensitive with dz than dx and dy . The inundation distance was shorter with $dz = 1.2$ m (blue lines) and longer with $dz = 0.8$ m (red lines). To give an overview, the inundation width and inundation distance were convergent as $dz < 1.2$ m.

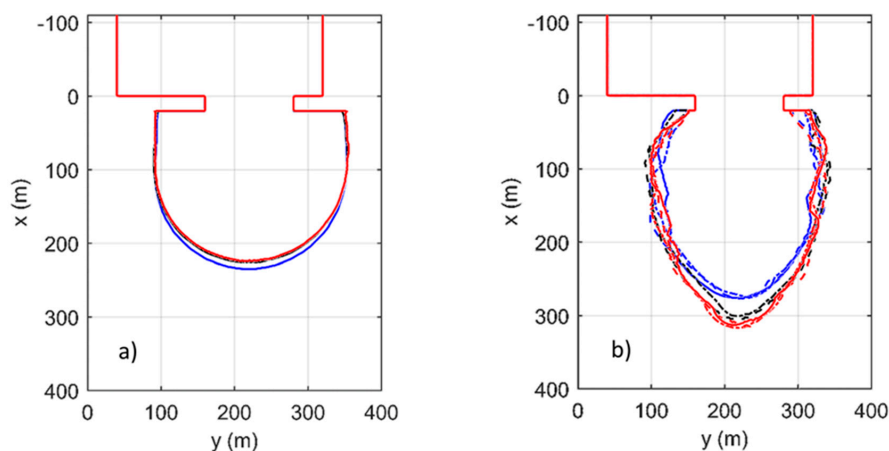


Figure 14. The stoppage boundary profiles of FGT66 for grid resolution analysis. (a) Bingham model (BM); (b) modified bi-viscosity model (MBM). Red lines: $dz = 0.8$; black lines: $dz = 1.0$; blue lines: $dz = 1.2$; solid lines: $dx = dy = 1.8$; dashed lines: $dx = dy = 2.0$; dash-dot lines: $dx = dy = 2.2$.

5.2. The Role of the Yield Strain Rate

In MBM, the yield strain rate $\dot{\gamma}_y$ defined the fluid behavior in the regime of un-yield and yield zones. If the yield strain rate was zero, the material returned to Bingham fluid. As the yield strain rate became higher, the plug zone became wider. The fluid was harder to transfer from un-yield to yield phases. The behavior of the tailings was not monotone when $\dot{\gamma}_y$ increased. There were two kinds of behavior of the tailings, presented in Figure 15. In the regime of $0.0 \leq \dot{\gamma}_y \leq 0.3 \text{ s}^{-1}$, the result shows that when $\dot{\gamma}_y$ increased, the inundation widths were narrower and the inundation lengths were longer. In the regime of $0.3 \leq \dot{\gamma}_y \leq 0.6 \text{ s}^{-1}$, when $\dot{\gamma}_y$ increased, not only were the inundation widths narrower, the inundation lengths were also shorter as well.

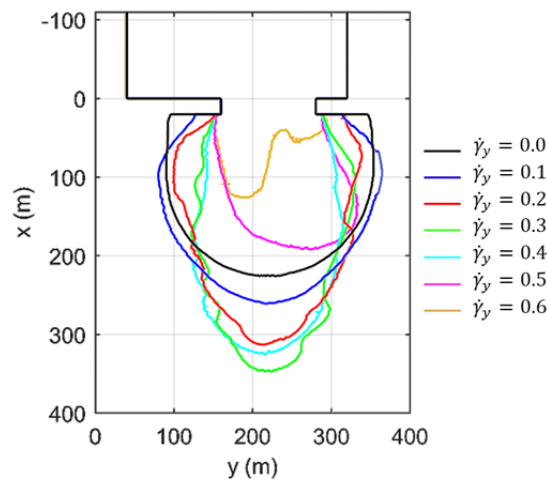


Figure 15. The stoppage boundary profiles of FGT66 predicted by the modified bi-viscosity model (MBM) for sensitivity analysis of yield strain rate $\dot{\gamma}_y$ (unit: s^{-1}).

Rheological properties of hyper-concentration are generally formulated as a function of the fluid concentration. Julien [44] recommended empirical formulas with the exponential relationships for yield stress and viscosity at large concentrations of fines. The typical values of coefficients for different types of mud, clay, and lahar are presented in Table 2. Kaolinite and Typical soils are utilized to describe the features of BM and MBM in this section. Eighteen numerical cases, including nine Bingham cases and nine modified Bi-viscosity cases with different concentration C_v , are performed. The yield shear stress and the viscosity are presented in Table 3. The yield strain rate is specified as $\dot{\gamma}_y = 0.0 \text{ s}^{-1}$ for the Bingham cases and $\dot{\gamma}_y = 0.2 \text{ s}^{-1}$ for the modified Bi-viscosity cases. The goal of this analysis is to find a material, which has a similar property to the tailings in FGT66. A similar inundation profile is the key. Figure 16 shows the simulation results with different concentration C_v by BM and MBM. The deposited boundary of Kaolinite at $C_v = 0.5$ (red line in Figure 16b) has the best fit to the MBM result of FGT66 (red line in Figure 15). It is due to the similarity of τ_y between two materials: Kaolinite $\tau_y = 1580 \text{ Pa}$ and the gypsum tailings $\tau_y = 1500 \text{ Pa}$.

Table 2. Coefficients of the yield stress (yield shear stress) and viscosity relationships [44].

Material	Liquid Limit C_v	Yield Stress in Pa: $\tau_y = a10^{bc_v}$		
		Viscosity in Pa s: $\mu_B = 0.001 \times 10^{cc_v}$		
		a	b	c
Bentonite	0.05–0.2	0.002	100	100
Sensitive clays	0.35–0.6	0.3	10	5
Kaolinite	0.4–0.5	0.05	9	8
Typical soils	0.65–0.8	0.005	7.5	8
Granular material	-	-	2	3

Table 3. The yield stress and yield viscosity of kaolinite and typical soils.

	Kaolinite					Typical Soils			
C_v	0.42	0.44	0.46	0.48	0.5	0.65	0.7	0.75	0.8
Yield stress	301.28	456.00	690.19	1.04×10^3	1.58×10^3	374.95	889.14	2.11×10^3	5000.00
Yield viscosity	2.29	3.31	4.79	6.92	10.00	158.49	398.11	1000.00	2.51×10^3

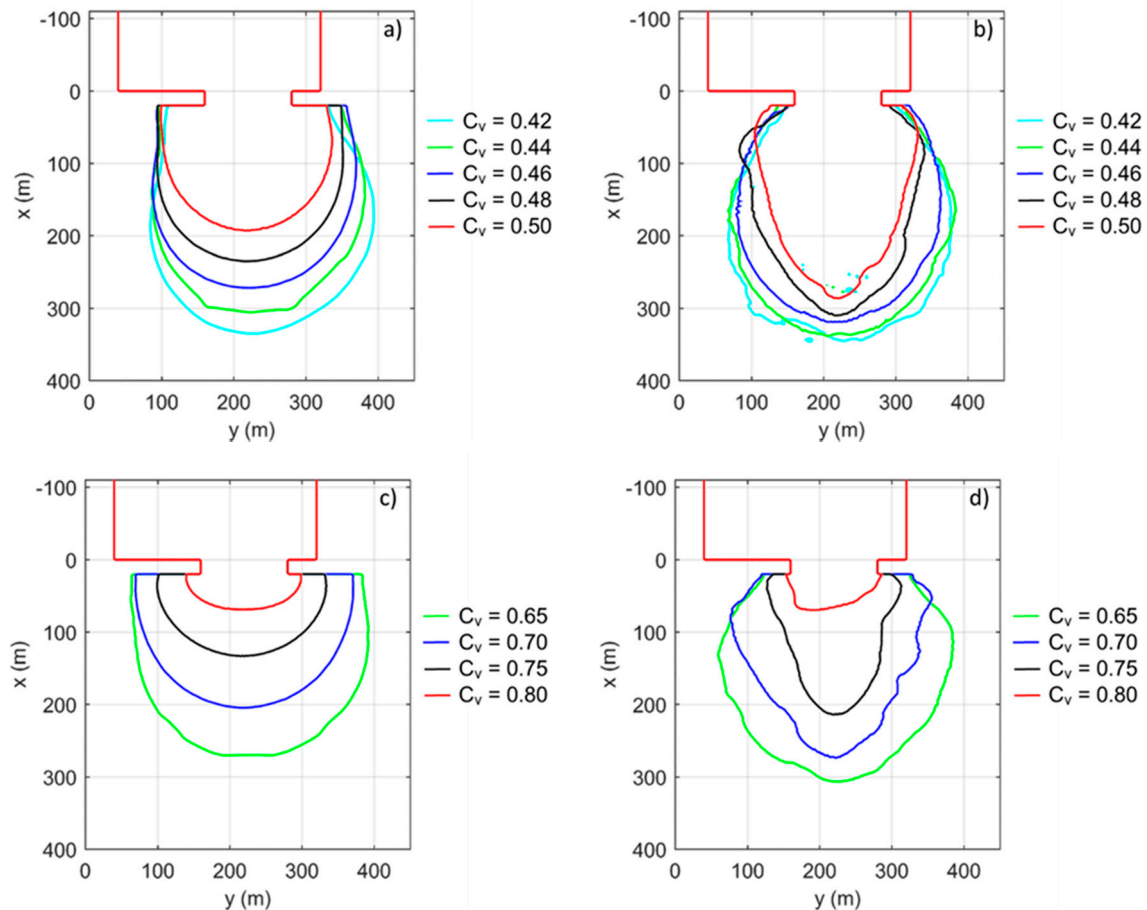


Figure 16. The stoppage boundary profiles for sensitivity analysis of concentration C_v . (a) Kaolinite simulated by BM; (b) kaolinite simulated by MBM; (c) typical soils simulated by BM; (d) typical soils simulated by MBM.

6. Conclusions and Future Work

This study applied the rheology models, BM, CBM, and MBM, to the mudslide simulation. The rheology models were integrated into the 3D Navier–Stokes equations coupled with the LES turbulent model to give a detailed description of the vertical acceleration. The free-surface kinematic was described by the VOF method with a PLIC surface tracking scheme. The BM results were validated by the channel flow and the spreading slow data, which received good agreements in both cases.

The Bingham model (BM) and conventional bi-viscosity model (CBM) were then used to simulate FGT66. The predicted inundation distance was 220 m with accuracy at about 73% of the observed data. To improve the result, a modification to CBM was raised. A large viscosity number of un-yield region, $\mu_A = 10^{10}$ Pa s, was applied to representing a more rigid behavior of the material as suggested by Assier Rzadkiewicz [34], Taibi [45], and Yu [28]. A series of sensitivity analyses on the yield strain rate $\dot{\gamma}_y$ was performed by matching the simulated tailings’ boundary to the field observation. A larger yield strain rate indicated the tailings with sturdier behavior. The yield strain rate was suggested to be

$\dot{\gamma}_y = 0.2 \text{ s}^{-1}$ in the MBM to simulate the FGT66. By the sensitivity analysis, the material of FGT66 was close to the kaolinite with concentration $C_v = 0.5$. The results show that the modified bi-viscosity model (MBM) could provide a better prediction than BM and CBM in terms of the flood distance and the spreading width. The development of the flood free-surface, velocity, strain rate, and un-yield/yield zone were presented and discussed.

The important results and conclusions are listed as follows:

- The Bingham model was successfully integrated into the 3D CFD model to simulate a mudslide by adopting the implicit scheme for the viscosity term;
- If the yield strain was small enough, the conventional bi-viscosity model would converge into the Bingham model numerically;
- The flood distance predicted by BM and CBM was 220 m, with the accuracy at about 73% of the field observation;
- To improve the result, MBM was introduced by giving a large viscosity to the un-yield phase and adjusting the yield strain rate with a sensitivity analysis;
- The flood distance predicted by MBM was 310 m, which was closer to the filed observation with 97% of the accuracy;
- Not only did the flood distance improve, the spreading width improved in the result of MBM;
- The free-surface, velocity, strain rate, and the un-yield/yield profiles were presented and discussed;
- The sensitivity analysis of the grid resolution was performed. The grid resolution in the BM was less sensitive than that in the MBM;
- The analysis of the yield strain rate was carried out. A larger yield strain rate indicated the tailings with sturdier behavior. The yield strain rate was suggested to be $\dot{\gamma}_y = 0.2 \text{ s}^{-1}$ in the MBM in the case of FGT66;
- The un-yield zone in MBM was sturdier than that in the pure BM. However, once tailings material yielded, the rheology returned to the conventional Bingham liquefied properties;
- By the sensitivity analysis, the material of FGT66 was close to the kaolinite with concentration $C_v = 0.5$.

This work is the Part I of modeling the slump-type landslide tsunamis. The Bingham-type rheology model was developed to simulate slumps and tailings flows. Model validation and sensitivity analysis were performed. Tsunamis excited by slumps will be studied in Part II.

Author Contributions: Conceptualization: T.-R.W. and T.-H.-N.V.; methodology: T.-R.W. and T.-H.-N.V.; software: T.-R.W., T.-H.-N.V., and C.-W.L.; validation: T.-H.-N.V.; writing—original draft preparation: T.-R.W. and T.-H.-N.V.; writing—review and editing: T.-R.W. and T.-H.-N.V.; visualization: T.-H.-N.V.; supervision: T.-R.W., C.-Y.W., and C.-R.C. All authors have read and agreed to the published version of the manuscript.

Funding: This research was funded by the Ministry of Science and Technology (MOST), Taiwan, grant number 107-2116-M-008-012 and the Centre of Excellence for Ocean Engineering, National Taiwan Ocean University.

Acknowledgments: The research leading to these results has received funding from the Ministry of Science and Technology (MOST), Taiwan, under the project number: 107-2116-M-008-012, and the Centre of Excellence for Ocean Engineering, National Taiwan Ocean University.

Conflicts of Interest: The authors declare no conflict of interest.

References

1. How Do Landslides Cause Tsunamis? Available online: https://www.usgs.gov/faqs/how-do-landslides-cause-tsunamis?qt-news_science_products=0#qt-news_science_products (accessed on 25 June 2020).
2. Grilli, S.T.; Tappin, D.R.; Carey, S.; Watt, S.F.L.; Ward, S.N.; Grilli, A.R.; Engwell, S.L.; Zhang, C.; Kirby, J.T.; Schambach, L.; et al. Modelling of the tsunami from the December 22, 2018 lateral collapse of Anak Krakatau volcano in the Sunda Straits, Indonesia. *Sci. Rep.* **2019**, *9*, 1–13. [CrossRef]
3. US Department of Commerce; NOAA, N.W.S. NWS JetStream—Tsunami Generation: Earthquakes. Available online: https://www.weather.gov/jetstream/gen_earth (accessed on 25 June 2020).

4. Liu, P.L.F.; Higuera, P.; Husrin, S.; Prasetya, G.S.; Prihantono, J.; Diastomo, H.; Pryambodo, D.G.; Susmoro, H. Coastal landslides in Palu Bay during 2018 Sulawesi earthquake and tsunami. *Landslides* **2020**, *17*, 2085–2098. [[CrossRef](#)]
5. Watts, P.; Grilli, S.T.; Kirby, J.T.; Fryer, G.J.; Tappin, D.R. Landslide tsunami case studies using a Boussinesq model and a fully nonlinear tsunami generation model. *Nat. Hazards Earth Syst. Sci.* **2003**, *3*, 391–402. [[CrossRef](#)]
6. Watts, P.; Grilli, S.T.; Tappin, D.R.; Fryer, G.J. Tsunami generation by submarine mass failure. II: Predictive equations and case studies. *J. Waterw. Port Coast. Ocean Eng.* **2005**, *131*, 298–310. [[CrossRef](#)]
7. Grilli, S.T.; Watts, P. Tsunami generation by submarine mass failure. I: Modeling, experimental validation and sensitivity analyses. *J. Waterw. Port Coast. Ocean Eng.* **2005**, *131*, 283–297. [[CrossRef](#)]
8. Jing, X.; Chen, Y.; Xie, D.; Williams, D.J.; Wu, S.; Wang, W.; Yin, T. The effect of grain size on the hydrodynamics of mudflow surge from a tailings dam-break. *Appl. Sci.* **2019**, *9*, 2474. [[CrossRef](#)]
9. Zhang, C.; Yang, C.H. Effect of fines content on liquefaction properties of tailings material. *Yantu Lixue/Rock Soil Mech.* **2006**, *27*, 1133–1137.
10. Qiao, L.; Qu, C.L.; Cui, M. Effect of fines content on engineering characteristics of tailings. *Yantu Lixue/Rock Soil Mech.* **2015**, *36*, 923–927. [[CrossRef](#)]
11. Schamber, D.R.; MacArthur, R.C. *One-Dimensional Model for Mud Flows*; ASCE: Orlando, FL, USA, 1985; pp. 1334–1339.
12. Liu, K.F.; Mei, C.C. Slow spreading of a sheet of Bingham fluid on an inclined plane. *J. Fluid Mech.* **1989**, *207*, 505–529. [[CrossRef](#)]
13. Liu, Y.; Balmforth, N.J.; Hormozi, S.; Hewitt, D.R. Two-dimensional viscoplastic dambreaks. *J. NonNewton. Fluid Mech.* **2016**, *238*, 65–79. [[CrossRef](#)]
14. Bates, B.M.; Ancey, C. The dam-break problem for eroding viscoplastic fluids. *J. NonNewton. Fluid Mech.* **2017**, *243*, 64–78. [[CrossRef](#)]
15. Huang, X.; García, M.H. A Herschel-Bulkley model for mud flow down a slope. *J. Fluid Mech.* **1998**, *374*, 305–333. [[CrossRef](#)]
16. Pudasaini, S.P.; Mergili, M. A Multi-Phase Mass Flow Model. *J. Geophys. Res.: Earth Surf.* **2019**, *124*, 2920–2942. [[CrossRef](#)]
17. Mitsoulis, E.; Tsamopoulos, J. Numerical simulations of complex yield-stress fluid flows. *Rheol. Acta* **2017**, *56*, 231–258. [[CrossRef](#)]
18. Jeyapalan, J.K.; Duncan, J.M.; Seed, H.B. Analyses of flow failures of mine tailings dams. *J. Geotech. Eng.* **1983**, *109*, 150–171. [[CrossRef](#)]
19. Pastor, M.; Quecedo, M.; González, E.; Herreros, M.I.; Merodo, J.A.F.; Fernández, J.A.; Mira, P. Simple approximation to bottom friction for Bingham fluid depth integrated models. *J. Hydraul. Eng.* **2004**, *130*, 149–155. [[CrossRef](#)]
20. Chen, S.C.; Peng, S.H. Two-dimensional numerical model of two-layer shallow water equations for confluence simulation. *Adv. Water Resour.* **2006**, *29*, 1608–1617. [[CrossRef](#)]
21. Harten, A.; Lax, P.D.; Leer, B. van On Upstream Differencing and Godunov-Type Schemes for Hyperbolic Conservation Laws. *Siam Rev.* **1983**, *25*, 35–61. [[CrossRef](#)]
22. Strang, G. On the Construction and Comparison of Difference Schemes. *Siam J. Numer. Anal.* **1968**, *5*, 506–517. [[CrossRef](#)]
23. Han, Z.; Su, B.; Li, Y.; Wang, W.; Wang, W.; Huang, J.; Chen, G. Numerical simulation of debris-flow behavior based on the SPH method incorporating the Herschel-Bulkley-Papanastasiou rheology model. *Eng. Geol.* **2019**, *255*, 26–36. [[CrossRef](#)]
24. Khattri, K.B.; Pudasaini, S.P. Channel flow simulation of a mixture with a full-dimensional generalized quasi two-phase model. *Math. Comput. Simul.* **2019**, *165*, 280–305. [[CrossRef](#)]
25. Li, Y.; Gong, J.H.; Zhu, J.; Ye, L.; Song, Y.Q.; Yue, Y.J. Efficient dam break flood simulation methods for developing a preliminary evacuation plan after the Wenchuan Earthquake. *Nat. Hazards Earth Syst. Sci.* **2012**, *12*, 97–106. [[CrossRef](#)]
26. Mergili, M.; Mergili, M.; Jaboyedoff, M.; Pullarello, J.; Pudasaini, S.P. Back calculation of the 2017 Piz Cengalo-Bondo landslide cascade with ravaflow: What we can do and what we can learn. *Nat. Hazards Earth Syst. Sci.* **2020**, *20*, 505–520. [[CrossRef](#)]

27. Henriquez, J.; Simms, P. Dynamic imaging and modelling of multilayer deposition of gold paste tailings. *Miner. Eng.* **2009**, *22*, 128–139. [[CrossRef](#)]
28. Yu, D.; Tang, L.; Chen, C. Three-dimensional numerical simulation of mud flow from a tailing dam failure across complex terrain. *Nat. Hazards Earth Syst. Sci.* **2020**, *20*, 727–741. [[CrossRef](#)]
29. Von Boetticher, A.; Turowski, J.M.; McArdell, B.W.; Rickenmann, D.; Hürlimann, M.; Scheidl, C.; Kirchner, J.W. DebrisInterMixing-2.3: A finite volume solver for three-dimensional debris-flow simulations with two calibration parameters—Part 2: Model validation with experiments. *Geosci. Model Dev.* **2017**, *10*, 3963–3978. [[CrossRef](#)]
30. Lee, E.S.; Violeau, D.; Issa, R.; Ploix, S. Application of weakly compressible and truly incompressible SPH to 3-D water collapse in waterworks. *J. Hydraul. Res.* **2010**, *48*, 50–60. [[CrossRef](#)]
31. Wang, W.; Chen, G.; Han, Z.; Zhou, S.; Zhang, H.; Jing, P. 3D numerical simulation of debris-flow motion using SPH method incorporating non-Newtonian fluid behavior. *Nat. Hazards* **2016**, *81*, 1981–1998. [[CrossRef](#)]
32. O'Brien, J.S.; Julien, P.Y.; Fullerton, W.T. Two-dimensional water flood and mudflow simulation. *J. Hydraul. Eng.* **1993**, *119*, 244–261. [[CrossRef](#)]
33. Noh, W.F.; Woodward, P. SLIC (Simple Line Interface Calculation). In Proceedings of the 5th International Conference on Numerical Methods in Fluid Dynamics, Technische Hogeschool Twente, Enschede, The Netherlands, 28 June–2 July 1976; pp. 330–340.
34. Assier Rzadkiewicz, S.; Mariotti, C.; Heinrich, P. Numerical simulation of submarine landslides and their hydraulic effects. *J. Waterw. Port Coast. Ocean Eng.* **1997**, *123*, 149–157. [[CrossRef](#)]
35. Dai, Z.; Huang, Y.; Cheng, H.; Xu, Q. 3D numerical modeling using smoothed particle hydrodynamics of flow-like landslide propagation triggered by the 2008 Wenchuan earthquake. *Eng. Geol.* **2014**, *180*, 21–33. [[CrossRef](#)]
36. Griffiths, R.W. The Dynamics of Lava Flows. *Annu. Rev. Fluid Mech.* **2000**, *32*, 477–518. [[CrossRef](#)]
37. McDougall, S.; Hungr, O. A model for the analysis of rapid landslide motion across three-dimensional terrain. *Can. Geotech. J.* **2004**, *41*, 1084–1097. [[CrossRef](#)]
38. Scheuner, T.; Schwab, S.; McArdell, B.W. Application of a two-dimensional numerical model in risk and hazard assessment in Switzerland. In Proceedings of the International Conference on Debris-Flow Hazards Mitigation: Mechanics, Prediction, and Assessment, Padua, Italy, 14–17 June 2011.
39. Christen, M.; Bühler, Y.; Bartelt, P.; Leine, R.; Glover, J.; Schweizer, A.; Graf, C.; McArdell, B.W.; Gerber, W.; Deubelbeiss, Y.; et al. Integral hazard management using a unified software environment. Numerical simulation tool “RAMMS” for gravitational natural hazards. In Proceedings of the 12th Congress INTERPRAEVENT, Grenoble, France, 23–26 April 2012; pp. 77–86.
40. Khabazi, N.P.; Taghavi, S.M.; Sadeghy, K. Peristaltic flow of Bingham fluids at large Reynolds numbers: A numerical study. *J. NonNewton. Fluid Mech.* **2016**, *227*, 30–44. [[CrossRef](#)]
41. Beverly, C.R.; Tanner, R.I. Numerical analysis of three-dimensional Bingham plastic flow. *J. NonNewton. Fluid Mech.* **1992**, *42*, 85–115. [[CrossRef](#)]
42. Kattel, P.; Khattri, K.B.; Pokhrel, P.R.; Kafle, J.; Tuladhar, B.M.; Pudasaini, S.P. Simulating glacial lake outburst floods with a two-phase mass flow model. *Ann. Glaciol.* **2016**, *57*, 349–358. [[CrossRef](#)]
43. Mergili, M.; Fischer, J.T.; Krenn, J.; Pudasaini, S.P. r. avaflow v1, an advanced open-source computational framework for the propagation and interaction of two-phase mass flows. *Geosci. Model Dev.* **2017**, *10*, 553–569. [[CrossRef](#)]
44. Julien, P.Y. *Erosion and Sedimentation*, 2nd ed.; Cambridge University Press: Cambridge, UK, 2010.
45. Taibi, H.; Messelmi, F. Effect of yield stress on the behavior of rigid zones during the laminar flow of Herschel-Bulkley fluid. *Alex. Eng. J.* **2018**, *57*, 1109–1115. [[CrossRef](#)]
46. Lam, K.; Tippetts, T.B.; Allen, D.W. Verification and Validation for induction heating. In Proceedings of the International Modal Analysis Conference XXV11, Orlando, FL, USA, 9–12 February 2009.
47. Coussot, P.; Proust, S. Slow, unconfined spreading of a mudflow. *J. Geophys. Res. Solid Earth* **1996**, *101*, 25217–25229. [[CrossRef](#)]
48. Eymard, R.; Gallouët, T.; Herbin, R. *Finite Volume Methods*; Elsevier: Amsterdam, The Netherlands, 2000.
49. Byron-Bird, R.; Dai, G.C.; Yarusso, B.J. Rheology and flow of viscoplastic materials. *Rev. Chem. Eng.* **1983**, *1*, 1–70. [[CrossRef](#)]
50. Chu, C.R.; Wu, T.R.; Tu, Y.F.; Hu, S.K.; Chiu, C.L. Interaction of two free-falling spheres in water. *Phys. Fluids* **2020**, *32*, 033304. [[CrossRef](#)]

51. Deardorff, J.W. A numerical study of three-dimensional turbulent channel flow at large Reynolds numbers. *J. Fluid Mech.* **1970**, *41*, 453–480. [[CrossRef](#)]
52. Blight, G.E. Destructive mudflows as a consequence of tailings dyke failures. *Proc. Inst. Civ. Eng. Geotech. Eng.* **1997**, *125*, 9–18. [[CrossRef](#)]
53. Smagorinsky, J. General circulation experiments with the primitive equations. *Mon. Weather Rev.* **1963**, *91*, 99–164. [[CrossRef](#)]
54. Hirt, C.W.; Nichols, B.D. Volume of fluid (VOF) method for the dynamics of free boundaries. *J. Comput. Phys.* **1981**, *39*, 201–255. [[CrossRef](#)]
55. Wu, T.R.; Liu, P.L.F. Numerical study on the three-dimensional dambreak bore interacting with a square cylinder. *Sel. Pap. Symp. Held Honor Philip L-F Lius 60th Birthd. Nonlinear Wave Dyn.* **2009**, 281–303. [[CrossRef](#)]
56. Wu, T.-R. A Numerical Study of Three-Dimensional Breaking Waves and Turbulence Effects. Ph.D. Thesis, Cornell University, New York, NY, USA, 2004.
57. Chorin, A.J. A numerical method for solving incompressible viscous flow problems. *J. Comput. Phys.* **1997**, *135*, 118–125. [[CrossRef](#)]
58. Chorin, A.J. Numerical Solution of the Navier-Stokes Equations. *Math. Comput.* **1968**, *22*, 745–762. [[CrossRef](#)]
59. Shao, S.; Lo, E.Y.M. Incompressible SPH method for simulating Newtonian and non-Newtonian flows with a free surface. *Adv. Water Resour.* **2003**, *26*, 787–800. [[CrossRef](#)]
60. Jeyapalan, J.K.; Duncan, J.M.; Seed, H.B. Investigation of flow failures of tailings dams. *J. Geotech. Eng.* **1983**, *109*, 172–189. [[CrossRef](#)]
61. Pastor, M.; Quecedo, M.; Fernández Merodo, J.A.; Herreros, M.I.; González, E.; Mira, P. Modelling tailings dams and mine waste dumps failures. *Geotechnique* **2002**, *52*, 579–591. [[CrossRef](#)]



© 2020 by the authors. Licensee MDPI, Basel, Switzerland. This article is an open access article distributed under the terms and conditions of the Creative Commons Attribution (CC BY) license (<http://creativecommons.org/licenses/by/4.0/>).